Lock-in rate-window thermomodulation (thermal wave) and photomodulation spectrometry

Andreas Mandelis and Zhuohui Chen
Photothermal and Optoelectronic Diagnostics Laboratory, and Ontario Laser and Lightwave Research Center, Department of Mechanical Engineering, University of Toronto, Toronto M5S 1A4, Canada

(Received 18 November 1991; accepted for publication 13 January 1992)

The application of the rate-window concept, familiar from deep level transient spectroscopy, to thermomodulation and photomodulation problems via lock-in detection has been investigated. Theoretical analysis of the newly adapted technique to these problems is presented and experimental photopyroelectric and photomodulated optical reflectance results are discussed. The utilization of the lock-in analyzer as a signal transient filtering system and as a dual-gate boxcar integrator equivalent with transient thermal wave signals is examined. Optimal instrumental conditions for use with thermal and electron-hole plasma analysis methodologies are presented, and experimental results with aluminum foil, crystalline and ion-implanted Si illustrate the potential of this measurement methodology for nondestructive thermal and electronic spectrometric evaluation of condensed phases and electronic materials.

I. INTRODUCTION

The technique of deep level transient spectroscopy (DLTS) has been successfully applied to the study of several types of semiconductors[1] and has measured the thermal emission properties of deep levels of impurities and defects.[1,2] In its conventional realization DLTS gives a measurement of the thermal electron population lifetime constant of, say, a junction by monitoring the capacitance transient following the application of an electrical[2] or optical[3,4] pulse across the junction. The time constant is determined by comparison with an electronically established "rate window," using a dual-gated boxcar integrator, the gates of which are adjusted through synchronization with respect to the end of the excitation pulse. Thus, for an exponential decay of lifetime τ, such as the carrier recombination in a specific defect level in a semiconductor

$$x(t) = e^{-t/\tau}. \tag{1}$$

Once the boxcar gates are fixed and set at times t_1 and t_2, the output signal can be written

$$\Delta S(t) = e^{-t_1/\tau} - e^{-t_2/\tau}, \tag{2}$$

with a maximum occurring for a carrier decay time constant, $\tau_{\max}$, such that $d(\Delta S)/d\tau = 0$, or

$$\tau_{\max} = \frac{t_2 - t_1}{\ln(t_2/t_1)}. \tag{3}$$

In DLTS the external parameter which varies the physical decay constant τ is the equilibrium temperature T of the junction. The inverse of $\tau_{\max}$ is the "rate window." Another, less popular method for establishing rate windows is using the lock-in analyzer instead of a boxcar integrator.[5–7] This method has recently been recognized to be very attractive for use with thermomodulation and photomodulation-generated signals,[8] as it is well suited for measuring the frequency content of thermal transients with a superior signal-to-noise ratio (SNR) to conventional transient photothermal detection schemes, due to the extremely narrowband filtering effected by commercially available lock-in analyzers.

In this work we report an instrumental lock-in rate window analysis of thermomodulation and photomodulation transients in the form of preliminary experimental results and theoretical analysis of the specific case of photopyroelectric (PPE) detection. Thus we obtain a quantitative understanding of the range of physical thermal and/or electronic transport lifetimes measurable by this methodology.

II. TRANSIENT THERMOMODULATION SIGNAL ANALYSIS

As a specific thermomodulation response, photopyroelectric (PPE) signal detection[9] following optical pulsing of a homogeneous sample by laser irradiation is a procedure quite similar to optical DLTS signal generation.[3,4,10] With PPE detection the thermal conduction transient buildup (decay) is monitored during (after the end of) the excitation pulse. With DLTS detection the electrical transient is always monitored after the end of the pulse. For a one-dimensional geometry as shown in Fig. 1, an optical impulse of fluence I_0[W/cm^2] and of the form

$$I(x,t) = I_0\delta(x)\delta(t) \tag{4}$$

has been shown[11] to produce in a thin polyvinylidene fluoride (PVDF) pyroelectric film a general thermal transit impulse response $T(x,t)$. In the special case where the sample is a good thermal conductor (such as crystalline semiconductor or some metals) and furthermore if the sample of thickness l and thermal diffusivity α_2 is thermally thin, i.e.,

 0034-6748/92/052977-12$02.00

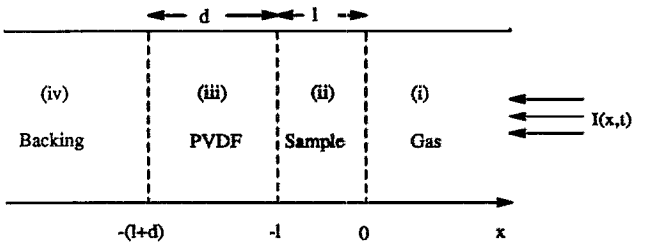

FIG. 1. Schematic of a four-layer one-dimensional photopyroelectric system.

$$\frac{l}{\sqrt{\alpha_2}} \ll \frac{d}{\sqrt{\alpha_3}} \tag{5}$$

(where d and α_3 are the thickness and the thermal diffusivity of the PVDF detector), the Laplace transform of the thermal impulse is given by[11]

$$\hat{T}(s) = 2\frac{I_0}{d}\left(\frac{\alpha_3}{\alpha_2}\right)^{1/2} \sum_{n=0}^{\infty} \left(\frac{e^{-(2n+1)q_2 l}}{s}\right). \tag{6}$$

In Eq. (6) s is the Laplace variable and $q_2 = (s/\alpha_2)^{1/2}$. $\hat{T}(s)$ can be considered the transform of the Green's function for the system in Fig. 1 in the thermally thin limit. For an optical pulse of fluence I_0 and duration τ_p, its Laplace transform is

$$\hat{I}(s) = I_0(1 - e^{-s\tau_p})/s. \tag{7}$$

Now the PPE *voltage* response to a finite duration pulse is given by multiplying the Laplace transforms, Eqs. (6) and (7) and inverting. In order to obtain the PPE *current* response, our experimental quantity, the time derivative of the inverse transform must be obtained[11]

$$i(t) = \frac{pd}{\epsilon}\frac{\partial}{\partial t}\overline{T(t)}, \tag{8}$$

where p and ϵ are the pyroelectric coefficient and the dielectric constant, respectively, of the PVDF detector, and $\overline{T}(t)$ is the detector thickness averaged temperature. The result is

$$\hat{i}(s) = \frac{pd}{\epsilon} I_0(1 - e^{-s\tau_p}) \sum_{n=0}^{\infty} \frac{e^{-(2n+1)q_2 l}}{s},$$

or, upon inversion[12]

$$i(t) = A\begin{cases} \displaystyle\sum_{n=0}^{\infty} \operatorname{erfc}\left(\frac{(2n+1)l}{2\sqrt{\alpha_2 t}}\right); & t < \tau_p \quad (9a) \\ \displaystyle\sum_{n=0}^{\infty} \left[\operatorname{erfc}\left(\frac{(2n+1)l}{2\sqrt{\alpha_2 t}}\right) - \operatorname{erfc}\left(\frac{(2n+1)l}{2\sqrt{\alpha_2 (t-\tau_p)}}\right)\right]; & t > \tau_p \quad (9b) \end{cases}$$

where

$$A \equiv (pd/\epsilon)I_0. \tag{10}$$

Now let us consider the PPE transient of Eq. (9) for several values of the thermal characteristic time constant

$$\tau_t \equiv l^2/4\alpha_2. \tag{11}$$

Figure 2 shows the effect of τ_t and τ_p on these transients.

Figure 2(a)(i) shows the thermal transients (both rise and decay) with different thermal characteristic time constants τ_t, and Fig. 2(a)(ii) shows the same thermal decay transients triggering at the end of the excitation pulse and normalized to the $t = 0$ value. Materials with different τ_t will have very different thermal transients. Figures 2(b)(i) and (ii) show the thermal transients of the same material (a single τ_t) but with different excitation pulse widths τ_p. It can be seen that the excitation pulse width τ_p does not change the behavior of the thermal rise profile, but it does affect somewhat the thermal decay transient.

III. LOCK-IN RATE-WINDOW METHODOLOGIES

A. Transient signal input

In thermomodulation and photomodulation experiments the input signal to the lock-in analyzer is a transient function, which in the PPE case above is given as

$$e_1(t) = i(t). \tag{12}$$

In Fig. 3 the electronic circuitry of a standard lock-in analyzer is shown.[13] $e_1(t)$ is the transient signal input; $e_2(t)$ is the mixer drive input, a square wave given by

$$e_2(t) = \begin{cases} 1; & -\dfrac{T_r}{2} + t_\theta \leqslant t \leqslant t_\theta \\ -1; & t_\theta \leqslant t \leqslant \dfrac{T_r}{2} + t_\theta \end{cases}, \tag{13}$$

where T_r is the period of the square wave, related to the lock-in reference angular frequency ω_r by

$$\omega_r = 2\pi/T_r = 2\pi f_r, \tag{14}$$

and t_θ is related to the lock-in phase setting θ_r by

$$t_\theta = T_r(\theta_r/2\pi). \tag{15}$$

$e_3(t)$ is the output of the heterodyning mixer:

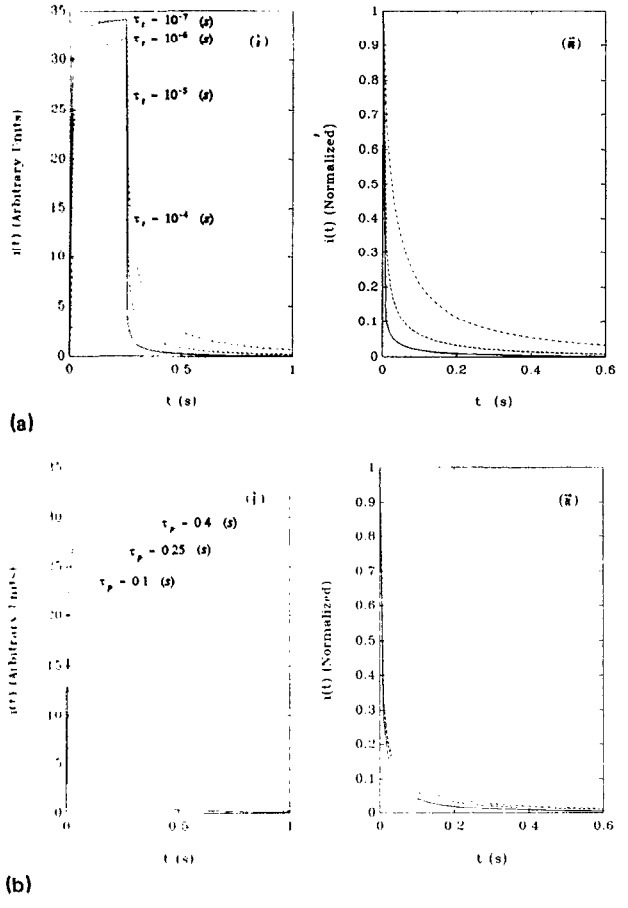

FIG. 2. (a) Photopyroelectric current response of the system in Fig. 1 with τ_t as a parameter; (i) Thermal rise profile and (ii) thermal decay profile after the end of the laser pulse: (—) $\tau_t = 10^{-7}$ s; (---) $\tau_t = 10^{-6}$ s; (-·-) $\tau_t = 10^{-5}$ s; and (···) $\tau_t = 10^{-4}$ s. (b) Same as (a) with τ_p as a parameter: (—) $\tau_p = 0.1$ s; (---) $\tau_p = 0.25$ s; and (-·-) $\tau_p = 0.4$ s.

$$e_3(t) = e_1(t)e_2(t), \tag{16}$$

and $e_4(t)$ is the signal output past the lowpass filter of time constant $\tau_L = RC$. This filter is assumed to have a transfer function $H(\omega,\tau_L)$.

A Fourier series expansion of the thermal pulse may be written assuming excitation pulse repetition rate $1/T_0$, Fig. 4(a):

$$i(t) = i(t + T_0), \tag{17}$$

so that

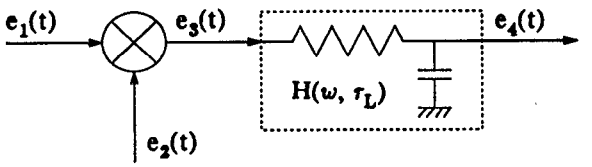

FIG. 3. Phase-sensitive detection (PSD) of lock-in analyzer simplified circuitry, (Ref. 13) including detection signal sequence: input signal $e_1(t)$, reference signal $e_2(t)$, mixer output $e_3(t)$, and lock-in output, bandpass filtered signal, $e_4(t)$.

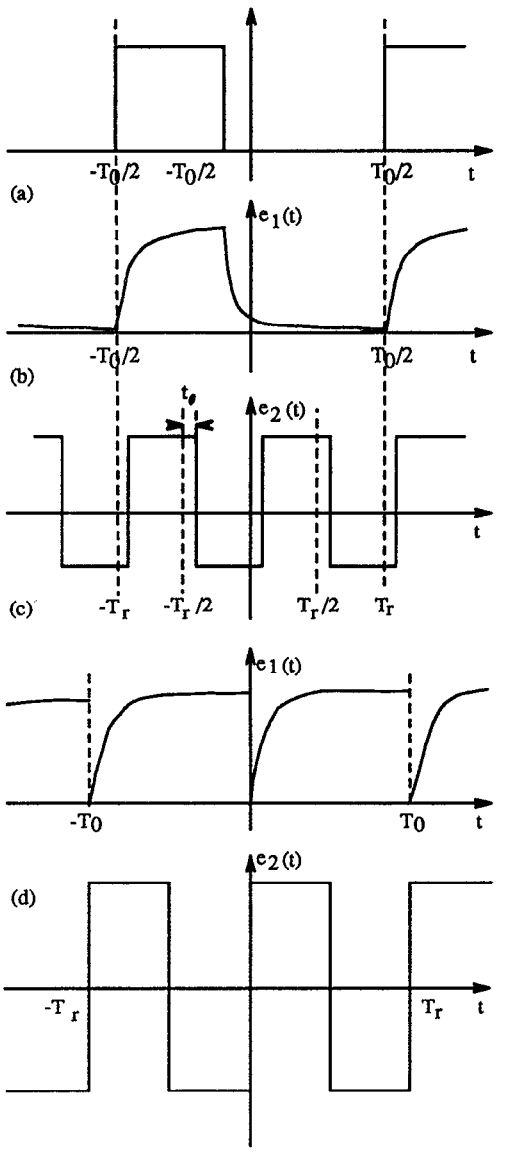

FIG. 4. (a) Optical excitation pulse-train of the photopyroelectric system of Fig. 1. (b) Transient photothermal signal-input to the lock-in analyzer. (c) Lock-in analyzer mixer weighing function with phase setting time offset $t_\theta \neq 0$ and period T_r. (d) Special case with $T_r = T_0$ and $t_\theta = 0$.

$$i(t) = \frac{1}{2}a_0 + \sum_{m=1}^{\infty}\left[a_m \cos\left(\frac{2\pi mt}{T_0}\right) + b_m \sin\left(\frac{2\pi mt}{T_0}\right)\right] \tag{18a}$$

$$= \frac{1}{2}a_0 + \sum_{m=0}^{\infty} c_m \sin\left(\frac{2\pi mt}{T_0} + \phi_m\right), \tag{18b}$$

where:

$$c_m = \sqrt{a_m^2 + b_m^2}, \quad \phi_m = \tan^{-1}\left(\frac{a_m}{b_m}\right). \tag{19}$$

Considering only the rising component of the signal [i.e., $t < \tau_p$ in Eq. 9(a); the decay profile, Eq. (9b), can be

treated identically and contains entirely equivalent information], we may write for the situation described in Fig. 4(b):

$$a_0 = \frac{2}{T_0} \sum_{n=0}^{\infty} \int_0^{T_0} \operatorname{erfc} \sqrt{\tau_n / t}\, dt, \tag{20a}$$

$$a_0 = 2 \sum_{n=0}^{\infty} \left[\operatorname{erfc} \sqrt{\tau_n / T_0} - \frac{2}{\sqrt{\pi}} \left(\frac{\tau_n}{T_0} \right) \left(\frac{e^{-\tau_n / T_0}}{\sqrt{\tau_n / T_0}} - \sqrt{\pi} \operatorname{erfc} \sqrt{\tau_n / T_0} \right) \right], \tag{20b}$$

$$a_m = \frac{2}{T_0} \sum_{n=0}^{\infty} \int_0^{T_0} \operatorname{erfc} \sqrt{\tau_n / t} \cos\left(\frac{2\pi m t}{T_0} \right) dt, \tag{21a}$$

or

$$a_m = \frac{1}{2m\pi} \sum_{n=0}^{\infty} \operatorname{Im}[F_m^{(n)}(T_0)], \tag{21b}$$

$$b_m = \frac{2}{T_0} \sum_{n=0}^{\infty} \int_0^{T_0} \operatorname{erfc} \sqrt{\tau_n / t} \sin\left(\frac{2\pi m t}{T_0} \right) dt, \tag{22a}$$

or

$$b_m = \frac{1}{2m\pi} \sum_{n=0}^{\infty} \{ \operatorname{Re}[F_m^{(n)}(T_0)] - 2 \operatorname{erfc} \sqrt{\tau_n / T_0} \}, \tag{22b}$$

where integration by parts of Eqs. (20a), (21a), and (22a) results in the representations (20b), (21b), and (22b) of the Fourier coefficients (See Appendix I). Furthermore, the rest of the symbols in the above equations are:

$$F_m^{(n)}(T_0) = e^{-\tau_n / T_0} [W(z_1) + W(z_2)]. \tag{23}$$

Here the complex function $W(z)$ is defined as

$$W(z) \equiv \exp(z^2) \operatorname{erfc}(z) \tag{24}$$

and

$$z_1 \equiv (z_1)_{m,n} = \sqrt{\frac{\tau_n}{T_0}} + (1 + i) \sqrt{m\pi} \tag{25a}$$

$$z_2 \equiv (z_2)_{m,n} = \sqrt{\frac{\tau_n}{T_0}} - (1 + i) \sqrt{m\pi}. \tag{25b}$$

Finally,

$$\tau_n \equiv (2n + 1)^2 \tau_t, \tag{26}$$

where τ_t is the thermal time constant of Eq. (11).

Appendix II gives algebraic expressions and ranges of validity for $W(z)$ across the complex plane ranges covered by all possible values of z_1 and z_2. Figure 5 shows the excellent fidelity of the reconstruction of $i(t)$ from its Fourier expansion, Eq. (18). For this reconstruction direct numerical integrations of Eqs. (20a), (21a), and (22a) were found to give better results than Eqs. (20b), (21b), and (22b), respectively, which exhibited an oscillatory envelope due to the accumulated round-off errors over all the terms n ($n_{\max} = 35$), for each of which a number $m_{\max} \sim O(100)$ was required for the $W(z)$ values to become independent of m. It was thus found that $n \gg 35$ was needed to improve the reconstruction fidelity, which made numerical integration attractive in terms of computer time for this particular situation.

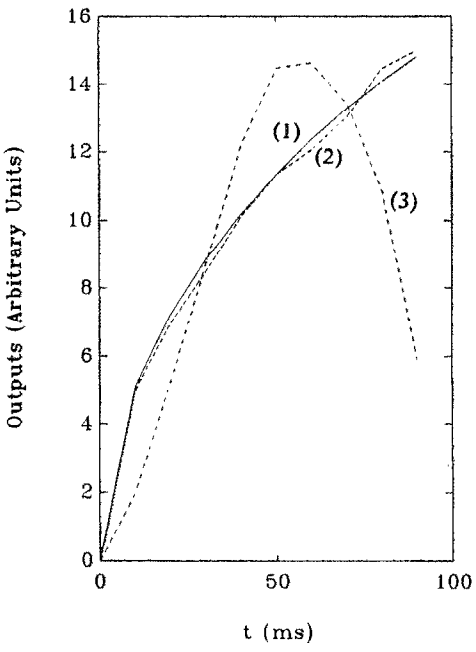

FIG. 5. Fourier series reconstruction (curve 2) $e_1(t) = i(t)$, Eq. (9a), with $t < \tau_p$ (curve 1). Parameters chosen for the simulation: $l = 100\ \mu$m, $\alpha_2 = 0.82\ \text{cm}^2/\text{s}$, $\tau_t = 3.048 \times 10^{-5}$ s, $f_0 = 5$ Hz. Number of Fourier coefficients: $m_{\max} = 35$; number of terms used in the numerical calculation of each Fourier coefficient: $n_{\max} = 35$. Curve (3) shows the behavior of $e_4(t)$, Eq. (33), with $\tau_L = 1$ ms. $T_r = T_0 = 100$ ms.

B. Heterodyning mixer output

The mixer drive input, Eq. (13), is a square wave as shown in Fig. 4(c) with Fourier series expansion[13]

$$e_2(t) = \frac{4}{\pi} \sum_{n=0}^{\infty} \frac{1}{2n+1} \sin[(2n+1)(\omega_r t + \theta_r)], \tag{27}$$

where θ_r is the lock-in phase setting, appearing in Eq. (15). Conventionally,[5,7,17–19] the lock-in analyzer has been used with DLTS signals as a rate-window instrument upon setting the transient pulse duration frequency (T_0^{-1}) equal to the reference frequency $f_r = T_r^{-1}$. Therefore, the lock-in rate window consists of selecting the fundamental Fourier component of the input signal transient. In a more general sense, it is important to investigate the effects of $T_r \neq T_0$ in transient thermal wave spectrometry, since slow, diffusive transients can produce time-dependent lock-in outputs, which may be affected advantageously by the low-pass filtering action of the instrument, in terms of SNR. It is well-known that the lock-in does not normally comprise the optimum SNR filter for transient signals,[17] but a correlation method does.[18] In view of the above remarks, we consider the form of the *entire* input transient $e_1(t)$ at the mixer output, after mixing (i.e., multiplication) with the fundamental Fourier component of the reference waveform $e_2(t)$:

$$e_3(t)=\frac{2}{\pi}\left(a_0\sin\left(\frac{2\pi}{T_r}t+\theta_r\right)+\sum_{m=1}^{\infty}c_m\left\{\cos\left[\frac{2\pi}{T_r}\left(m\frac{T_r}{T_0}-1\right)t+\phi_m-\theta_r\right]-\cos\left[\frac{2\pi}{T_r}\left(m\frac{T_r}{T_0}+1\right)t+\phi_m+\theta_r\right]\right\}\right). \tag{28}$$

C. Band-pass filtered output

Two kinds of low-pass filters will be considered for the lock-in analyzer:[13] an ideal, infinitely sharp cutoff filter with noise bandwidth $f_N = f_L$, and a real filter with $f_N > f_L$ ($f_L = 1/2\pi\tau_L$ is the signal bandwidth). Assuming filter transfer function $H(\omega,\tau_L)$, the lock-in output $e_4(t)$ can be written as a convolution integral:

$$e_4(t)=e_3(t)*F^{-1}[H(\omega,\tau_L)], \tag{29}$$

where the inverse Fourier transform of the $H(\omega,\tau_L)$ indicates the impulse response of the filter. For ideal filtering

$$H_{\text{ideal}}(\omega,\tau_L)=\begin{cases}1; & \omega\leqslant\omega_L\equiv 2\pi f_L\\ 0; & \omega>\omega_L\end{cases}. \tag{30}$$

In terms of the rectangle function $\Pi(x)$, defined by[20]

$$\Pi(x)=\begin{cases}1; & |x|\leqslant 1/2\\ 0; & |x|>1/2\end{cases}, \tag{31}$$

we may also write

$$H_{\text{ideal}}(\omega,\tau_L)=\Pi[(f/f_L)-1/2]. \tag{32}$$

The convolution operation in Eq. (29) shifts the origin of the filter frequency-domain window for each component of the $e_3(t)$ expansion, so that finally we obtain for the b_m-proportional (odd Fourier) series:

$$e_4(t)^{(\text{odd})}_{(\text{ideal})}=\frac{2}{\pi}\sum_{m=1}^{\infty}b_m\left\{\Pi\left[\left(m\frac{T_r}{T_0}-1\right)\frac{\tau_L}{T_r}-\frac{1}{2}\right]\times\cos\left[\frac{2\pi}{T_r}\left(m\frac{T_r}{T_0}-1\right)t-\theta_r\right]-\Pi\left[\left(m\frac{T_r}{T_0}+1\right)\frac{\tau_L}{T_r}-\frac{1}{2}\right]\times\cos\left[\frac{2\pi}{T_r}\left(m\frac{T_r}{T_0}+1\right)t+\theta_r\right]\right\}. \tag{33}$$

Similar expressions can be obtained for the rest of terms in Eq. (18a). When real filtering is considered, it is most convenient to use a Lorentzian filter:

$$H_{\text{real}}(\omega,\tau_L)=\frac{1}{1+i\omega\tau_L}, \tag{34}$$

such that

$$F^{-1}[H_{\text{real}}(\omega,\tau_L)]=\frac{1}{\tau_L}\begin{cases}e^{-t/\tau_L}; & t>0\\ 0; & t<0\end{cases}. \tag{35}$$

After convolution in the time-domain we obtain:

$$e_4(t)^{(\text{odd})}_{(\text{real})}=\frac{2}{\pi}\sum_{m=1}^{\infty}b_m\,\text{Re}\left(\frac{\exp\left\{i\left[\frac{2\pi}{T_r}\left(m\frac{T_r}{T_0}-1\right)t-\theta_r\right]\right\}}{1+2\pi i\left(m\frac{T_r}{T_0}-1\right)\frac{\tau_L}{T_r}}-\frac{\exp\left\{i\left[\frac{2\pi}{T_r}\left(m\frac{T_r}{T_0}+1\right)t+\theta_r\right]\right\}}{1+2\pi i\left(m\frac{T_r}{T_0}+1\right)\frac{\tau_L}{T_r}}\right), \tag{36}$$

where

$$\text{Re}\left(\frac{e^{ix}}{1+iy}\right)=\frac{\cos x+y\sin x}{1+y^2}, \tag{37}$$

with similar expressions for the rest of the (even and constant) terms.

D. Special cases

Here we will consider two important special cases of lock-in outputs, depending on the filter time-constant setting τ_L.

1. Short filter time constant: $\tau_L \ll T_r$ or $f_L \gg f_r$

In this case the entire frequency content of $e_3(t)$ passes unattenuated through the filter, Fig. 2. In the limit $\tau_L = 0$, $\Pi(-1/2)=1$ and $\text{Re}[e^{ix}/(1+iy)] = \cos x$; $x = (2\pi/T_r)[m(T_r/T_0)\pm 1]t \pm \theta_r$. Equation (28) shows that the lock-in outputs the entire time-dependent waveform $e_3(t)$. For actual instruments (e.g., EG & G lock-in Model No. 5210) the minimum time constant is $(\tau_L)_{\min} = 1$ ms. Using this value, Fig. 5 curve (3) shows the shape of the waveform $e_4(t) \simeq e_3(t)$ for $0 \leqslant t \leqslant T_0/2$, with $e_1(t)$ given by curve (1) of the same figure. The maximum of the curve Fig. 5 curve (3) contains information about the transport time τ_t. Figure 6 shows a sequence of lock-in outputs representing thermomodulation transients with different thermal transport time constants τ_t, $0 \leqslant t \leqslant T_0/2$. A monotonic increase in the temporal position of $t_{\max}$ with τ_t indicates that, upon calibration, the lock-in output may be used to measure τ_t. The advantage of lock-in detection lies in the ability to vary τ_L so as to eliminate higher frequency components from Eq. (33) or Eq. (36) and thus substantially improve the SNR.

Due to the diffusive nature of thermomodulation signals, the energy content of the PPE response is heavily weighed towards the low frequencies. Therefore, the lock-in output is expected to vary dramatically with T_r changes, as the bandpass filter is centered at f_r.[13] Figure 7 shows

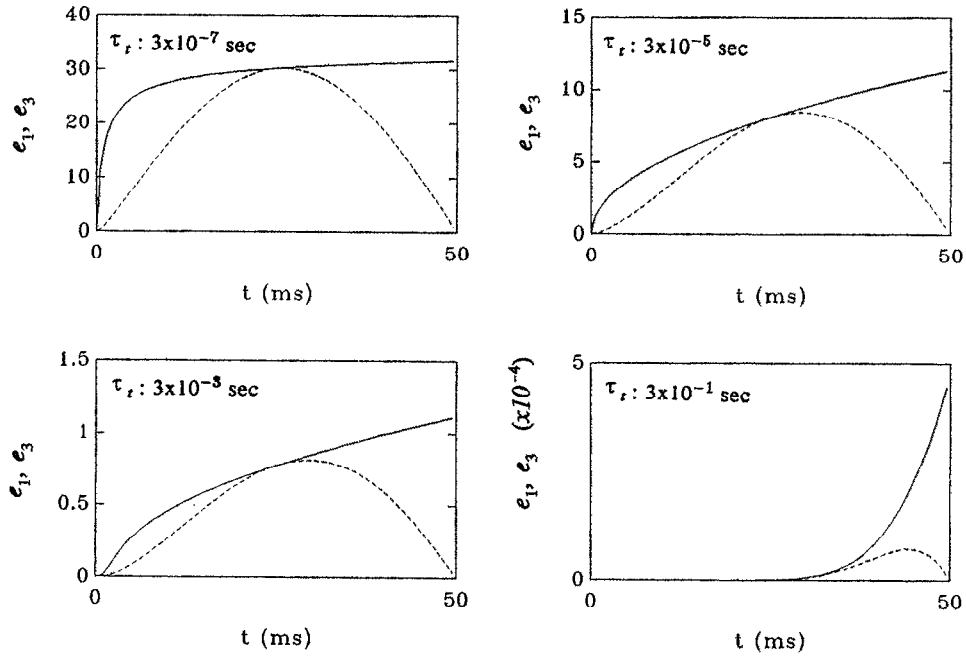

FIG. 6. Input thermomodulation waveforms (solid lines) and lock-in outputs (dashed lines) showing the maximum of the output response dependence on τ_t when $e_4(t) \simeq e_3(t)$. $\tau_L = 1$ ms, $T_0 = T_r = 100$ms.

experimental results from an aluminum foil sample using the geometry of Fig. 1 as described earlier.[21] The severe signal attenuation (pulse decay) with increased reference frequency is evident in that figure.

An alternative rate-window methodology with fast transient thermomodulation signals compared to the minimum lock-in filter time constant, $(\tau_L)_{\min}$, is to use conventional DLTS-type detection of the rise or the decay portion of the transient without the lock-in, and with the computer setting up narrow rate windows, i.e., replacing the dual-gated boxcar integrator. In the PPE current rise response case, Eq. (9a), the equivalent of Eq. (3) is

$$(\tau_t)_{\max} = \frac{1}{2}\left(\frac{t_1 t_2}{t_2 - t_1}\right)\ln(t_2/t_1), \tag{38}$$

assuming that $\tau_t > \max(t_1, t_2)$. Similarly, for the decay portion, Eq. (9b), $(\tau_t)_{\max} = \tau$ can be found numerically from the maximum condition:

$$t_1^{-1/2}e^{-\tau/t_1} - (t_1 - \tau_p)^{-1/2}e^{-\tau/(t_1-\tau_p)} = t_2^{-1/2}e^{-\tau/t_2} - (t_2 - \tau_p)^{-1/2}e^{-\tau/(t_2-\tau_p)}. \tag{39}$$

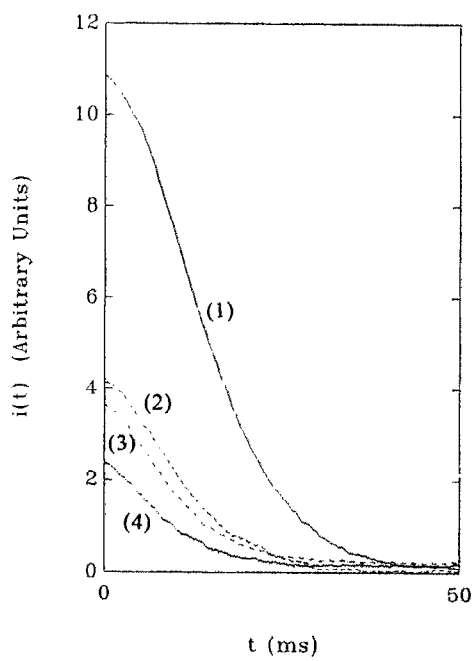

FIG. 7. PPE decay curves from a 30-μm-thick aluminum foil, following an optical pulse of duration $\tau_p = 20$ ms, using an EG & G Model 5210 lock-in with $\tau_L = 1$ ms. Reference frequency: (1) 400 Hz, (2) 600 Hz, (3) 800 Hz, and (4) 1 kHz.

Figure 8 shows a thermomodulation rate-window procedure for the decay portion of the aluminum foil PPE response of Fig. 7, without lock-in processing, which simulates the $\tau_L = 0$ case. It is convenient to notice that a pure exponential decay model fits the thermal decay curve [Fig. 8(a)] and the rate-window [Fig. 8(b)] very well. Thermal transit time τ_t measurements can be easily obtained from Fig. 8(b). At this time it appears that lock-in detection with short τ_L using the rate-window concept will primarily be qualitative (quantitative after proper calibration) in measuring τ_t, due to the experimentally observed strong effect of the value of T_r on the temporal peak position of the rate-windowed response.

Further qualitative insights into the usefulness of short filter time-constant lock-in thermomodulation and photomodulation rate-window transient detection have been derived using the modified photomodulated optical reflectance (PMOR) scheme[22–24] of Fig. 9, adapted for rate-window detection. An electrical pulse of duration τ, mixed with an ac ripple in the 2–100 kHz frequency range, described by

$$F(t) = \begin{cases} 1 + me^{i\omega_r t}; & 0 < t < \tau \\ 0; & t > \tau \end{cases}, \tag{40}$$

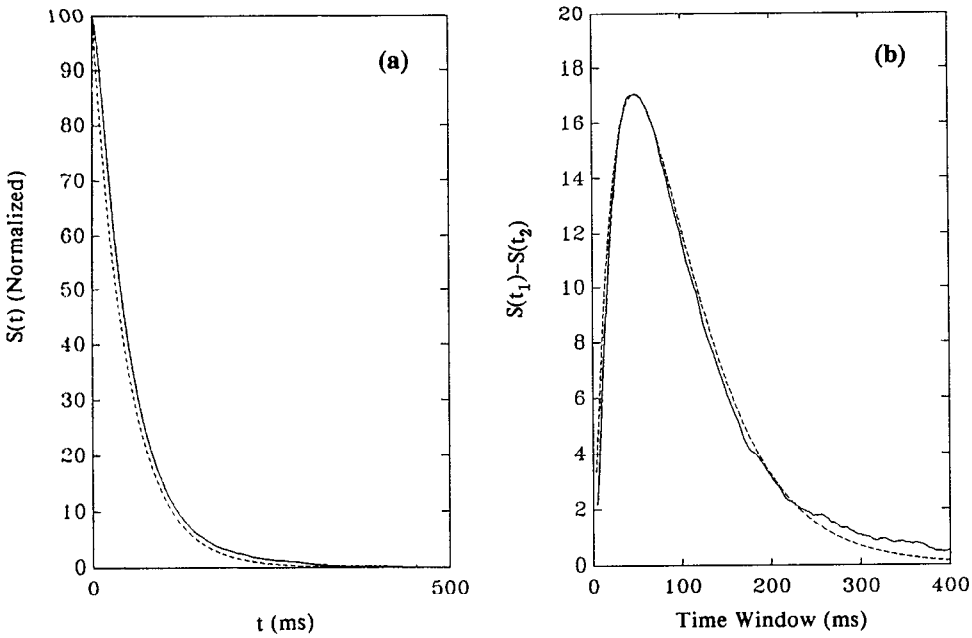

FIG. 8. PPE decay curve (a) and rate-window signal processing (b) of the thermomodulation signal from a 30-μm-thick Al foil without the lock-in analyzer. The solid lines are the data. The dashed line is the fit of the purely exponential decay model 100 exp($-t/$ 48.09 ms). Time windows are set at $t_2/t_1 = 1.5$.

with $m \ll 1$, is used as the input to the acousto-optic modulator (A/O). The 514-nm line of an Ar^+ ion laser is thus an intensity-modulated pulse of duration τ, typically 100 ms. Both pump and He-Ne 632.8-nm probe beam are focused collinearly on the sample surface. The detected reflected probe beam is directed to a Si photodetector in the conventional manner.[22–24] The detector output is connected to a phase-sensitive, two-channel lock-in amplifier with fast (ms) time constant and an electronic filter with frequency tracking capability. The lock-in is referenced at $f_r = \omega_r/2\pi$ and tracks the temporal evolution of the Fourier components of the photothermal response of the sample after the end of the optical pulse. The experimental system is controlled by an IBM PS/2 computer, which acts as a dual-gate integrator on the transient frequency signals. Using this "rate-window" method,[2] the transient in-phase or quadrature magnitude is sampled at two different times t_1 and t_2 after the pulse. The difference between the two signal levels at t_1 and t_2 is the output ΔS_I. For a given rate-window, signal (ΔS_I) scanning as a function of modulation frequency (f_r) produces a maximum at a characteristic frequency, ω_e, which depends on the thermal diffusivity and the pump beam spot size. This can be shown by direct analysis of the Fourier content of the thermal-wave problem with a laser source temporal behavior given by Eq. (40). Consideration of the three-dimensional thermal-wave problem gives[25]

$$\omega_e = \text{const.} \times \alpha_s / W^2, \tag{41}$$

where α_s is the thermal diffusivity and W^2 is the beam spotsize, assuming a Gaussian profile:

$$A(r) = \frac{\eta I_0}{\pi W^2 k_s} e^{-2r^2/W^2}. \tag{42}$$

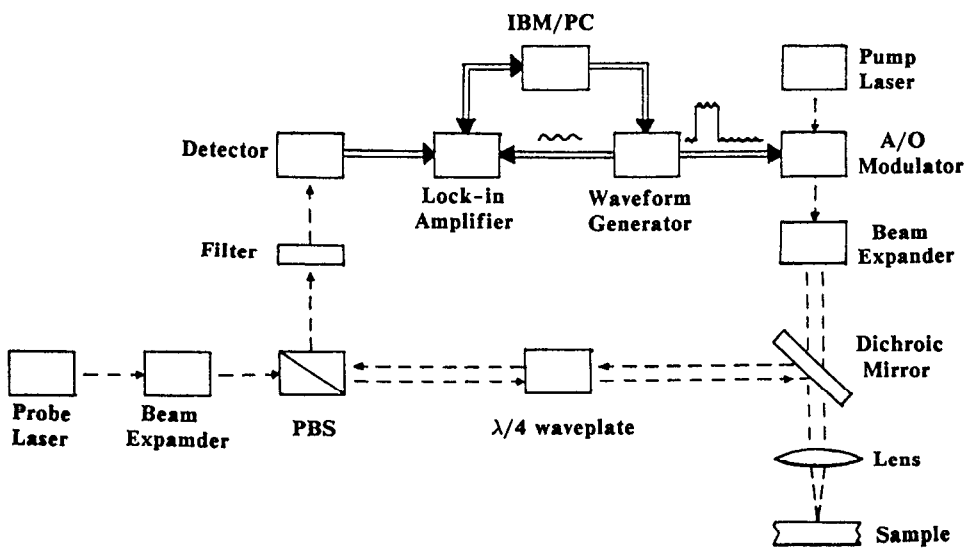

FIG. 9. The experimental setup for rate-window transient photomodulated optical reflectance (PMOR) spectrometry. An acousto-optically (A/O) modulated laser pulse is used as a pump beam and a two-channel lock-in analyzer with a fast filter time constant is employed to track the temporal evolution at the ac ripple frequency produced by the waveform generator.

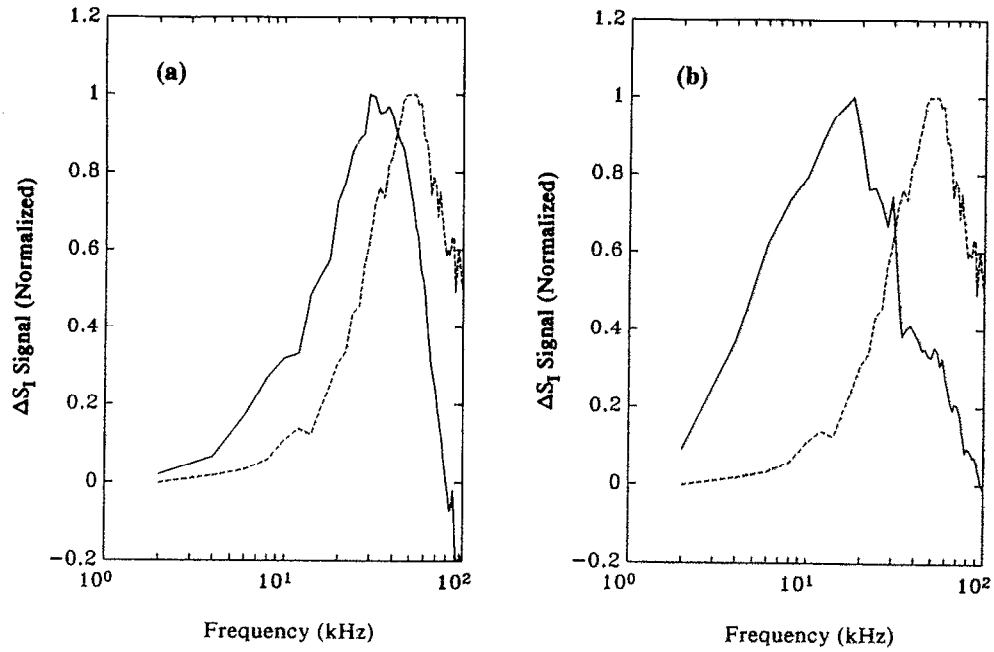

FIG. 10. (a) Rate-window PMOR spectra of crystalline Si with pump beam diameter 1 μm (dashed curve), and 30 μm (solid curve); (b) similar spectra of crystalline Si (dashed curve), and ion-implanted Si (solid curve). Pump laser beam diameter: 1 μm; Time window $t_2/t_1 = 1$ ms; $\tau_L = 1$ ms.

In Eq. (42), η is a nonradiative energy conversion efficiency, I_0 is the incident laser intensity, and k_s is the material thermal conductivity. An in-phase transient signal from a crystalline Si wafer sample of $f_r = 50$ kHz can thus be obtained. In the case of good thermal conductors, such as crystalline semiconductors, the frequency transient decay time constant is limited by the lock-in filter response time constant (1 ms); therefore, the time-gated signal produces information about the thermal diffusivity only through the magnitude of the transient. Results are shown in Fig. 10. Figure 10(a) shows in-phase experimental results from c-Si with the laser beam focused to different spotsizes. The frequency $f_e = \omega_e/2\pi$, which corresponds to the maximum ΔS_I signal, is 50 kHz when the pump beam is focused through a microscope objective to 1-μm-diam spot. The peak shifts down to 32 kHz when lens focusing is used to 30-μm beam spot size, in agreement with Eq. (41). Figure 10(b) shows similar in-phase results with the pump beam fixed at a spot diameter of 1 μm. The solid curve represents results from a P^+ implanted Si sample with a dose of 10^{16} cm^{-2} at 150-keV ion energy. The frequency f_e (16 kHz) is seen to be approximately one-third of that obtained with crystalline Si (50 kHz). In view of Eq. (41) these data can be interpreted that the thermal diffusivity α_s for our implanted Si sample is one-third of that for c-Si.

2. Long filter time constant: $\tau_L \gg T_r$

For either ideal or real-filter behavior, only the term $m(T_r/T_0) = 1$ in the expression(s) for $e_4(t)$ will survive [See Eqs. (33) and (36)]. If the ratio $T_r/T_0 = \omega_0/\omega_r$ is not an integer, then the closest term to $\mathrm{Int}(T_0/T_r)$ will be output by the lock-in analyzer. In the conventional DLTS applications $T_r = T_0$, so that the lock-in outputs the demodulated $m = 1$ term of $e_4(t)$ only, which is constant in time (a dc-level signal). For ideal filtering,

$$\Pi\left[\left(m\frac{T_r}{T_0}\pm 1\right)\frac{\tau_L}{T_r}-\frac{1}{2}\right]\to 0 \quad \text{as } \tau_L\to\infty,$$

except for $m = \mathrm{Int}(T_0/T_r)$, for which $\Pi(0-1/2)\to 1$. Therefore

$$e_4(t)_{\text{ideal}} = \frac{2}{\pi}c_{\mathrm{Int}(T_0/T_r)}\cos\theta_r. \tag{43}$$

The expression for $e_4(t)_{\text{real}}$ is the same as can be easily verified from Eq. (36). It can be shown that Eq. (43) is also the result of the conventional DLTS lock-in rate window treatment:[5] In DLTS the lock-in output is taken to be the integral of the product of the square-wave (reference) weighting function [Fig. 4(c)] and the fundamental Fourier component c_1 of the input signal. For PPE detection and assuming that $T_r \sim T_0$, so that $m = 1$, Eq. (43) indicates that

$$e_4(t) = \text{const.}\times c_1(\tau_t)\,(\text{time-independent}). \tag{44}$$

Figure 11(a) shows the frequency scanned thermal wave signal during the photothermal pulse buildup of Fig. 2(a)(i). A minimum for the amplitude output of the lock-in occurs when $(1/T_0)_{\max} = 8\times 10^{-5}\,1/\tau_t$. Therefore, the thermal characteristic time constant τ_t can be obtained from the frequency $(1/T_0)_{\max}$ corresponding to the maximum thermomodulation signal.

Figure 11(b) is the frequency scanned thermomodulation signal after the end of the photothermal pulse, corresponding to Fig. 2(a)(ii). This signal exhibits a maximum. As shown in Eq. (9b), this thermal transient is dependent on the value of τ_p. Therefore, for different τ_p, the transient behaves differently, Fig. 2(b). Figure 11(b) shows that the maximum of the frequency scanned thermomodulation signal varies with photothermal pulse width τ_p. Figure 12 shows the dependence of the maximum $\tau_t/(T_0)_{\max}$ of Fig. 11(b) on the pulse width τ_p/T_0. Since the ratio τ_p/T_0 is

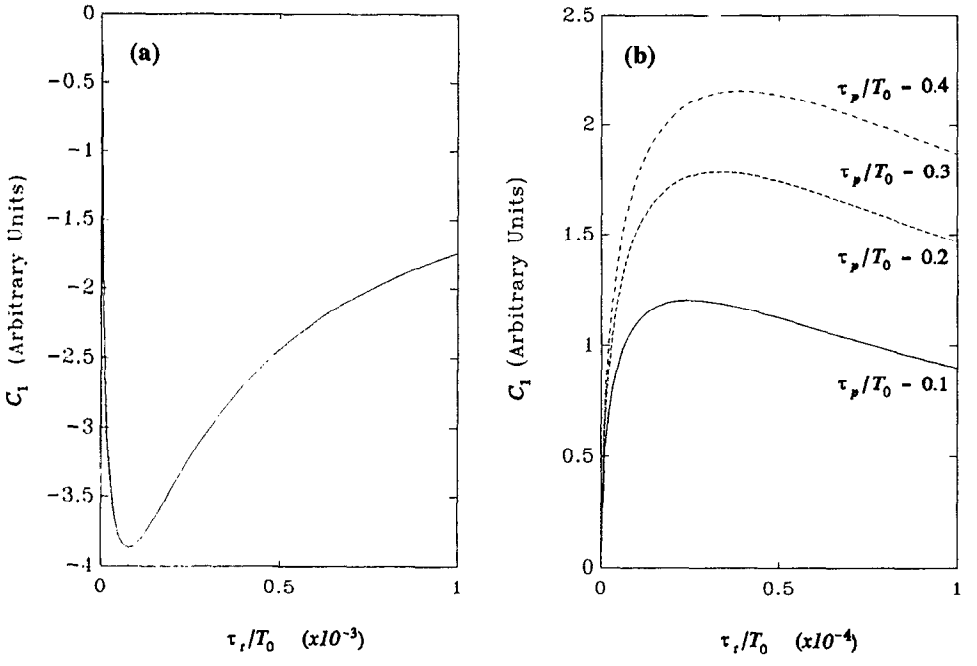

FIG. 11. (a) PPE signal fundamental Fourier component dependence on thermal (or electronic) transport time τ_t, during the build-up part of the transient in Fig. 2(a)(i). The minimum is observed upon scanning the lock-in reference frequency at $\tau_t/T_0 = 8 \times 10^{-5}$; (b) similar plots for the decay part of the transient in Fig. 2(a)(ii). The maximum is a function of pulse duration τ_p. $\tau_t/(T_0)_{max}$ is equal to 2.5×10^{-5} (—); 3.3×10^{-5} (---); 3.9×10^{-5} (-·-); and 4.3×10^{-5} (···). The ratio τ_p/T_0 is, respectively, 0.1, 0.2, 0.3, and 0.4. Lock-in constant $\tau_L \gg T_r$.

known from the experiment, one can obtain the thermal characteristic time constant τ_t using Fig. 12. Once a reference sample is used to calibrate this plot, measurements of the characteristic time constants τ_t of any other sample can be made using the same experimental method and the same lock-in rate-window setup. Adjustment of the lock-in phase for maximum signal output may be effected, which sets $\theta_r = 0$ in Eq. (43). The importance of Figs. 11 and 12 lies in their general validity for both one-dimensional thermomodulation (thermal diffusion time constants) and photomodulation (electron-hole plasma recombination time constants) lock-in rate-window measurements: different signal origins, such as PMOR generation, will only change the $c_1(\tau_t)$ functional dependence and a different plot from Fig. 11 will thus ensue. As far as PPE detection is concerned using the present methodology, Fig. 11 shows that upon using a long lock-in time constant τ_L, even with long pulse repetition periods and very low reference frequencies, fairly short system physical time constants τ_t can be accessed, with strong lock-in response levels, superior

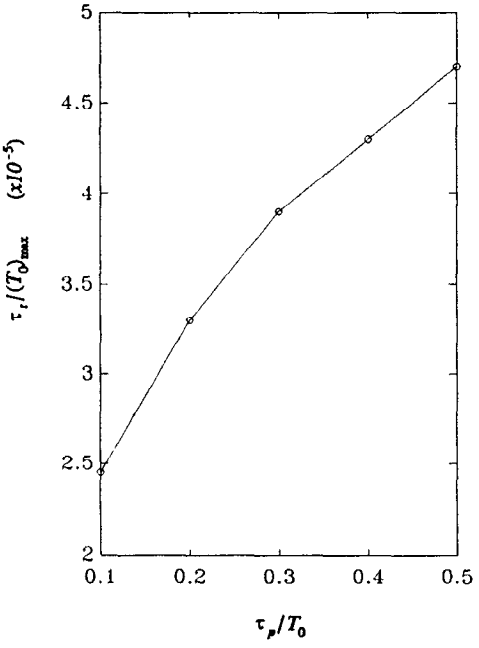

FIG. 12. Calibration curve of lock-in dc maximum output locus of Fig. 11(b). τ_p and T_0 are experimentally set. $(T_0)_{max}$ is the pulse repetition time which achieves the maximum lock-in output. τ_t can be readily determined from the curve.

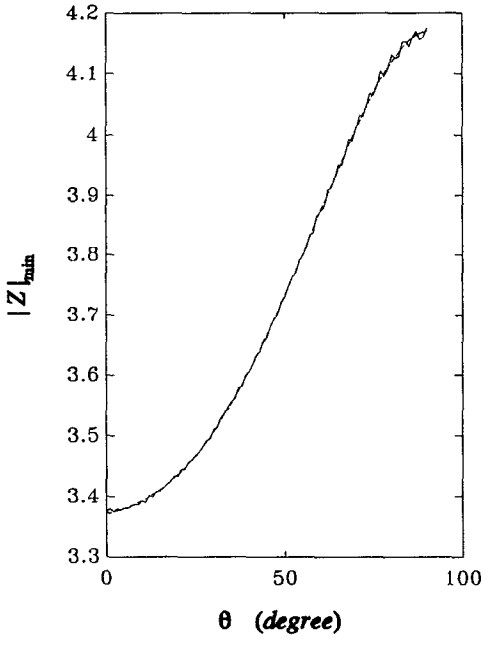

FIG. 13. Numerical curve (—) and polynomial fit (---) of the argument $|z|$ which produces the least error in making the transition from the Taylor formulas to the asymptotic expansions, Eqs. (A9), for the function $W(z) = \exp(z^2)\,\mathrm{erfc}(z)$. First quadrant is shown only: $0° \leqslant \theta \leqslant 90°$.

noise rejection, and excellent resolution down to a few μs. This ability of lock-in rate-window instrumentation methodologies is, therefore, very promising for semiconductor optoelectronic defect assessment, using sub-band-gap optical probing[26,27] for monitoring plasma kinetics [$\sim O(\mu s)$ relaxations] into defect states following super-band-gap excitation. Experimental implementation of this methodology to semiconductor diagnostics is under way and will be reported in a future publication.

ACKNOWLEDGMENTS

The support of the Ontario Laser and Lightwave Research Center (OLLRC) and the Natural Sciences and Engineering Research Council of Canada (NSERC) is gratefully acknowledged.

APPENDIX I

The integral $\phi(t)=\int_0^t dx/x^{3/2}\exp(-a^2/x-ib^2x)$:

The above integral occurs in the theory of Fourier expansions of diffusive signals, such as that generated in thermomodulation (heat diffusion) and photomodulation (carrier diffusion). As an example, Eq. (22a) when integrated by parts gives

$$b_m=\frac{T_0}{4m\pi}\sum_{n=0}^{\infty}\left\{\mathrm{Re}\left[\int_0^{T_0}\frac{dt}{t^{3/2}}\exp\left(-\frac{\tau_n}{t}-i\frac{2m\pi t}{T_0}\right)\right]-(-1)^m\,\mathrm{erfc}\sqrt{2\tau_n/T_0}\right\}. \tag{A1}$$

The integral on the right-hand side is the generalization to the complex plane of the integral

$$\int_0^t x^{-3/2}\exp\left(\frac{a^2}{x}-b^2x\right)dx,$$

the closed-form of which was given by Horenstein.[14] To evaluate $\phi(t)$ let $y^2=x^{-1}$, which yields

$$\phi(t)=2\int_{1/\sqrt{t}}^{\infty}\exp(-a^2y^2-ib^2/y^2)dy. \tag{A2}$$

Let $c\equiv t^{-1/2}$ and complete the square in the parentheses of Eq. (A2) thus obtaining:

$$\phi(t)=\exp[\sqrt{2}(1+i)ab]\times\int_c^{\infty}\exp\left\{-a^2\left[\left(y+\frac{b}{\sqrt{2}ay}\right)+i\frac{b}{\sqrt{2}ay}\right]^2\right\}dy. \tag{A3}$$

Set $\xi=ib/\sqrt{2}ay$, so that

$$\phi(t)=\left(\frac{ib}{\sqrt{2}a}\right)\exp[\sqrt{2}(1+i)ab]\int_{i0}^{ib/\sqrt{2}ac}\xi^{-2}\times\exp\left[-a^2\left(\frac{ib}{\sqrt{2}a\xi}+(1-i)\xi\right)^2\right]d\xi$$

$$=-\exp[\sqrt{2}(1+i)ab]\int_{i0}^{ib/\sqrt{2}ac}\left((1-i)-\frac{ib}{\sqrt{2}a\xi^2}\right)\times\exp\left[-a^2\left(\frac{ib}{\sqrt{2}a\xi}+(1-i)\xi\right)^2\right]d\xi+(1-i)\times\exp[\sqrt{2}(1+i)ab]\times\int_{i0}^{ib/\sqrt{2}ac}\exp\left[-a^2\left(\frac{ib}{\sqrt{2}a\xi}+(1-i)\xi\right)^2\right]d\xi.$$

Making the variable change $x=a(1-i)\xi+ib/\sqrt{2}\xi$ we finally obtain

$$\phi(t)=\exp[\sqrt{2}(1+i)ab]\left\{\frac{1}{a}\int_{ac+(1+i)b/\sqrt{2}c}^{\infty}e^{-x^2}dx+(1-i)\times\int_{i0}^{ib/\sqrt{2}ac}\exp\left[-a^2\left(\frac{ib}{\sqrt{2}a\xi}+(1-i)\xi\right)^2\right]d\xi\right\}. \tag{A4}$$

Note that Eq. (A3) may also be written as

$$\phi(t)=\exp[-\sqrt{2}(1+i)ab]\int_c^{\infty}\exp\left\{-a^2\left[\left(y-\frac{b}{\sqrt{2}ay}\right)-i\frac{b}{\sqrt{2}ay}\right]^2\right\}dy. \tag{A5}$$

Manipulations similar to those leading to Eq. (A4) yield:

$$\phi(t)=\exp[-\sqrt{2}(1+i)ab]\left\{\frac{1}{a}\int_{ac-(1+i)b/\sqrt{2}c}^{\infty}e^{-x^2}dx-(1-i)\int_{i0}^{ib/\sqrt{2}ac}\exp\left[-a^2\left(\frac{ib}{\sqrt{2}a\xi}-(1-i)\xi\right)^2\right]d\xi\right\}. \tag{A6}$$

Adding Eqs. (A4) and (A6) gives the expression:

$$\phi(t)=\frac{\sqrt{\pi}}{4a}\left\{\exp[\sqrt{2}(1+i)ab]\,\mathrm{erfc}\left[\left(\frac{a}{\sqrt{t}}-b\sqrt{\frac{t}{2}}\right)+ib\sqrt{\frac{t}{2}}\right]+\exp[-\sqrt{2}(1+i)ab]\,\mathrm{erfc}\left[\left(\frac{a}{\sqrt{t}}-b\sqrt{\frac{t}{2}}\right)-ib\sqrt{\frac{t}{2}}\right]\right\}. \tag{A7}$$

Using the parameters

$$a\equiv\sqrt{\tau_n};\quad b\equiv\sqrt{2m\pi/T_0},$$

Eq. (A7) when evaluated at $t=T_0$ yields Eq. (22b) with the definitions (23)–(25).

APPENDIX II

The function $W(z)=\exp(z^2)\,\mathrm{erfc}(z)$:

For numerical implementation of Eqs. (20b), (21b), and (22b) the complex function $W(z)$ was constructed and studied as a series expansion, a function of the complex plane angular coordinate θ. Using polar coordinates

$$z=|z|e^{i\theta} \tag{A8}$$

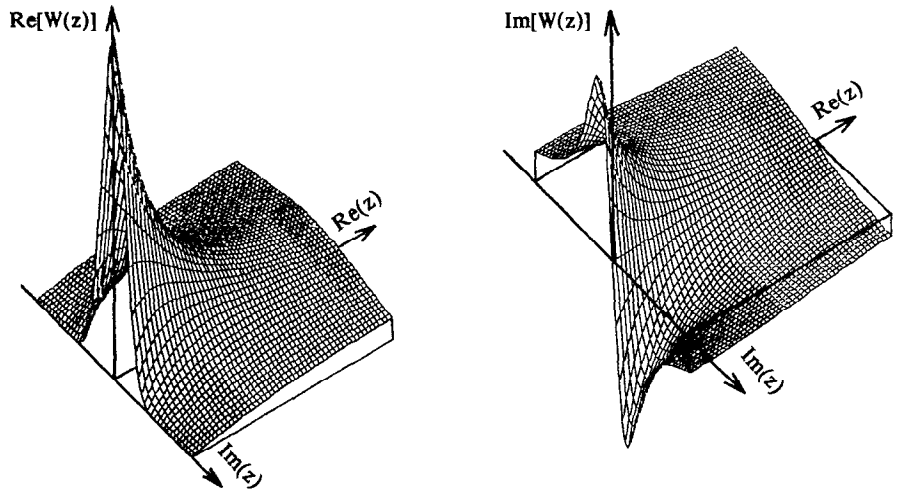

FIG. 14. Reliefs of Re[$W(z)$] and Im[$W(z)$] in the first and fourth quadrants: $-90°\leqslant\theta\leqslant 90°$. The curve/criterion of Fig. 13 was used for smooth transitions from Taylor to asymptotic expansions at all θ values.

for small values of the argument $|z|$ the Taylor expansions were constructed, while for large values of $|z|$ asymptotic formulas were used.[15] We summarize the pertinent formulas here and simplify earlier expressions:[15]

$$\mathrm{Re}[W(z)] = \begin{cases} \exp(|z|^2\cos 2\theta)\left\{\cos(|z|^2\sin 2\theta) - \dfrac{2}{\sqrt{\pi}}\displaystyle\sum_{n=0}^{\infty}(-1)^n\dfrac{|z|^{2n+1}\cos[|z|^2\sin 2\theta + (2n+1)\theta]}{n!(2n+1)}\right\} \text{ (Taylor)} \\ \dfrac{1}{\sqrt{\pi}}\displaystyle\sum_{n=0}^{\infty}(-1)^n\dfrac{(2n-1)!!\cos[(2n+1)\theta]}{2^n|z|^{2n+1}} \text{ (Asymptotic)}, \end{cases} \tag{A9a}$$

$$\mathrm{Im}[W(z)] = \begin{cases} \exp(|z|^2\cos 2\theta)\left\{\sin(|z|^2\sin 2\theta) - \dfrac{2}{\sqrt{\pi}}\displaystyle\sum_{n=0}^{\infty}(-1)^n\dfrac{|z|^{2n+1}\sin[|z|^2\sin 2\theta + (2n+1)\theta]}{n!(2n+1)}\right\} \text{ (Taylor)} \\ -\dfrac{1}{\sqrt{\pi}}\displaystyle\sum_{n=0}^{\infty}(-1)^n\dfrac{(2n-1)!!\sin[(2n+1)\theta]}{2^n|z|^{2n+1}} \text{ (Asymptotic)}. \end{cases} \tag{A9b}$$

A complete investigation of the $|z|_{\min}$ values at which the transition from Taylor to asymptotic expansions minimizes the difference between the two expressions was performed for the first time. An earlier approximate calculation[15] had yielded the point $|z| = 3.9$ at $\theta = 0$. Figure 13 shows the results for $0°\leqslant\theta\leqslant 90°$. A polynomial fit to the numerical curve was then produced and stored in the computer as the transition criterion for any θ. In view of the nature of the variables z_1 and z_2 in Eq. (25), negative values of the imaginary part of the argument corresponding to $\theta<0$ were easily handled by noting that

$$W(-z) = \exp(z^2)[2 - \mathrm{erfc}(z)] = 2e^{z^2} - W(z). \tag{A10}$$

Therefore,

$$\mathrm{Re}[W(-z)] = 2\exp(|z|^2\cos 2\theta)\cos(|z|^2\sin 2\theta) - \mathrm{Re}[W(z)], \tag{A11a}$$

$$\mathrm{Im}[W(-z)] = 2\exp(|z|^2\cos 2\theta)\sin(|z|^2\sin 2\theta) - \mathrm{Im}[W(z)]. \tag{A11b}$$

Figure 14 shows reliefs of real and imaginary parts of $W(z)$ in the first and fourth quadrants, covering the range $-90°\leqslant\theta\leqslant 90°$. This range is completely adequate for all z_1 and z_2 values in Eq. (25) and represents the first well-behaved such relief over half of the complex plane, to the authors' best knowledge. Earlier formulas for $W(z)$ exhibited continuity problems in switching expressions between adjacent sectors[15] ($-45°\leqslant\theta\leqslant 45°$ and $45°\leqslant\theta\leqslant 135°$) due to the lack of a continuous transition criterion as a function of θ, such as shown in Fig. 13, or the function became unbounded[16] for negative values of θ. The specific expressions in Eq. (A8) for the z_1, z_2 functions, Eqs. (25a) and (25b) are

$$|z_{1,2}| = \{[(\tau_n/T_0)^{1/2} \pm (m\pi)^{1/2}]^2 + m\pi\}^{1/2} \tag{A12}$$

and

$$\theta_{1,2} = \pm \tan^{-1}\left(\frac{(m\pi)^{1/2}}{(\tau_n/T_0)^{1/2} \pm (m\pi)^{1/2}}\right). \qquad \text{(A13)}$$

[1] D. V. Lang, in *Topics in Applied Physics*, edited by P. Bräunlich (Springer, New York, 1979), Vol. 37, Chap. 3.
[2] D. V. Lang, J. Appl. Phys. **45**, 3023 (1974).
[3] D. V. Lang, J. D. Cohen, and J. P. Harbison, Phys. Rev. B **25**, 5285 (1982).
[4] A. Chantre, G. Vincent, and D. Bois, Phys. Rev. B **23**, 5335 (1981).
[5] D. S. Day, M. Y. Tsai, B. G. Streetman, and D. V. Lang, J. Appl. Phys. **50**, 5093 (1979).
[6] J. T. Schott, H. M. Deangelis, and W. R. White, Air Force Cambridge Research Laboratories Rep. No. AFCRL-TR-76-0024 (1976).
[7] L. C. Kimerling, IEEE Trans. Nucl. Sci. **NS-23**, 1497 (1976).
[8] Z. Chen and A. Mandelis, Proc. 7th Int. Top. Meet. Photoacoustic and Photothermal Phenomena, Doorwerth, Holland (1991) (in press).
[9] H. Coufal and A. Mandelis, Ferroelectrics **118**, 379 (1991).
[10] Z. Chen and A. Mandelis, Appl. Phys. Lett. **59**, 1861 (1991).
[11] J. F. Power and A. Mandelis, Rev. Sci. Instrum. **58**, 2018 (1987).
[12] A. Mandelis and B. S. H. Royce, J. Appl. Phys. **50**, 4330 (1979).
[13] D. M. Munroe, *A Lock-in Amplifier Primer*, EG & G Princeton Applied Research Technical Publ. T459 (1986).
[14] W. Horenstein, Quart. Appl. Math. **3**, 183 (1945).
[15] A. Mandelis and B. S. H. Royce, J. Appl. Phys. **51**, 610 (1980).
[16] M. Abramowitz and A. Stegun, *Handbook of Mathematical Functions*, 9th ed., (National Bureau of Standards, Washington, D.C., 1970).
[17] G. L. Miller, D. V. Lang, and L. C. Kimerling, Ann. Rev. Mater. Sci. 377 (1977).
[18] G. L. Miller, J. V. Ramirez, and D. A. H. Robinson, J. Appl. Phys. **46**, 2638 (1975).
[19] P. M. Henry, J. M. Meese, J. W. Farmer, and C. D. Lamp, J. Appl. Phys. **57**, 628 (1985).
[20] R. Bracewell, *The Fourier Transform and its Applications* (McGraw-Hill, New York, 1965).
[21] I. A. Vitkin, S. B. Peralta, A. Mandelis, W. Sadowski, and E. Walker, Meas. Sci. Technol. **1**, 184 (1990).
[22] W. L. Smith, A. Rosencwaig, and D. Willenborg, Appl. Phys. Lett. **47**, 584 (1985).
[23] I. A. Vitkin, C. Christofides, and A. Mandelis, Appl. Phys. Lett. **54**, 2392 (1989).
[24] C. Christofides, I. A. Vitkin, and A. Mandelis, J. Appl. Phys. **67**, 2815 (1990).
[25] A. Mandelis and Z.-H. Chen (unpublished).
[26] S. J. Sheard and M. G. Somekh, Infrared Phys. **28**, 287 (1988).
[27] Z. G. Ling and P. K. Ajmera, J. Appl. Phys. **69**, 519 (1991).